https://doi.org/10.5194/egusphere-2026-812
Preprint. Discussion started: 23 February 2026

Potential of point source imaging satellite instruments to infer diffuse methane emissions: a theoretical case study of the Near-Infrared Multispectral Camera (NIMCAM)

Chlöe N. Schooling[1], Liang Feng[1,2], A. Jerome P. Woodwark[1], and Paul I. Palmer[1,2]

[1]School of GeoSciences, University of Edinburgh, United Kingdom
[2]National Centre for Earth Observation, University of Edinburgh, Edinburgh, United Kingdom

Corresponding author: Chlöe N Schooling (cschooli@ed.ac.uk), Paul I Palmer (pip@ed.ac.uk)

Abstract. Satellite measurements have revolutionized methane monitoring, yet persistent clouds and aerosols often limit global-survey instruments like TROPOMI in the tropics. This study evaluates the potential of the Near Infrared Multispectral Camera for Atmospheric Methane (NIMCAM), a high-resolution instrument (60 m pixels) designed for point sources, to quantify large-scale diffuse emissions across tropical Africa. Through closed-loop numerical experiments, we compare an in-orbit demonstrator and small NIMCAM constellations (2–5 satellites) against synthetic data from the TROPOMI (TROPOspheric Monitoring Instrument) instrument. Using Sentinel-2 cloud probabilities and downscaled MODIS aerosol optical depth products, we find that NIMCAM's finer spatial resolution significantly increases clear-sky data yields. A 5-satellite constellation provides up to six times more clear-sky observations than TROPOMI. As masking criteria for clouds and aerosols become more stringent, the ratio of NIMCAM to TROPOMI random error ($\sigma_{\mathrm{NIM}}/\sigma_{\mathrm{TROP}}$) decreases. This occurs because TROPOMI's coarser footprint leads to a more rapid loss of data under strict thresholds. Using the GEOS-Chem chemical transport model and an ensemble Kalman Filter, we demonstrate that NIMCAM observations offer substantial added value in resolving tropical emissions. NIMCAM achieves higher uncertainty reduction than TROPOMI, particularly in regions and seasons where cloud and aerosol loading restrict coarser instruments. Our findings support using high-resolution methane technology to complement global surveys in monitoring diffuse tropical emissions.

1 Introduction

Over the last decade, the atmospheric growth rate of methane has surged to record levels (Feng et al., 2022, 2023; Pendergrass et al., 2025; Ciais et al., 2026), challenging existing climate projections. This acceleration is driven by two poorly understood variables: a massive spike in natural tropical emissions and potential large-scale but unresolved changes in the hydroxyl radical, the primary loss of atmospheric methane (Turner et al., 2019; Zhang et al., 2023; Feng et al., 2023). Other lines of evidence indicate that rising anthropogenic emissions — including fossil fuel combustion, agriculture, and waste — have also contributed to the recent methane increase, although their magnitude relative to natural source variability and changes in the atmospheric sink remains uncertain and actively debated in the literature (Skeie et al., 2023; Saunois et al., 2025).

https://doi.org/10.5194/egusphere-2026-812
Preprint. Discussion started: 23 February 2026

The uncertainty surrounding these drivers is compounded by significant logistical and political barriers that now hinder the maintenance of ground-based monitoring networks in critical regions. Consequently, satellite-based remote sensing has become the backbone of methane research. Without space-borne observations, our ability to track shifting emissions across tropical wetlands and rapidly thawing high-latitude ecosystems would be virtually non-existent, leaving a dangerous blind spot in the global climate strategy. Since 2010, the two workhorses responsible for helping to monitor changes in atmospheric methane are the Japanese Greenhouse gases Observing SATellite (GOSAT) and the European TROPOspheric Monitoring Instrument (TROPOMI). However, the data from these instruments have spatial resolutions of several kilometres so that persistent clouds during wet seasons and elevated aerosol loading during dry season burning significantly reduces the number of clear-sky scenes (Qu et al., 2021; Balasus et al., 2023).

Meanwhile, there has been a rapid expansion of satellite instruments that have been designed, or have been repurposed, to observe small-scale point sources of methane, taking advantage sensitivity of methane in the shortwave infrared (SWIR) bands (Varon et al., 2021; Gorroño et al., 2023; Jervis et al., 2021; Mostafa and Du, 2025). Data from this class of instrument typically have spatial resolutions of tens of metres, so there is a higher probability of collecting data between clouds (Charuvil Asokan et al., 2025) and between regions of elevated aerosol loading. Recent work has shown that this type of data can influence emission estimates for both anthropogenic and natural emissions (Campbell et al., 2025). In this study we argue that while these newer instruments are less sensitive to methane, commensurate with diffuse sources of methane, the spatial resolution of their data and the co-addition of individual measurements can outperform the global survey instruments. We illustrate this using the Near Infrared Multispectral Camera for Atmospheric Methane (NIMCAM) mission concept (Woodwark et al., 2026), which has been designed specifically to locate and quantify emissions from large point-sources. For the purposes of our experiment, we consider an in-orbit demonstrator (IOD) and constellations that range from three to five NIMCAM instruments.

Our study is focused on tropical Africa. The region hosts extensive wetland systems that are seasonally dynamic and poorly monitored and is also undergoing rapid land-use change and population growth, potentially contributing to increasing anthropogenic methane sources (Bullock et al., 2021; Zhang et al., 2021). Studies have shown that large-scale methane emission increases in this region, can be attributed to changes in rainfall and subsequent wetland inundation (Lunt et al., 2019, 2021; Feng et al., 2022, 2023; Hardy et al., 2023). These studies have relied substantially on clear-sky data collected immediately downwind of emitting regions because of extensive cloud cover and biomass burning aerosol overhead of the emitting regions. This challenge is widespread across the humid tropics; Frankenberg et al. (2024) report very low satellite data yields due to persistent shallow cumulus clouds, with success rates of just 0.1–1.0% in the Amazon during the wet season. They further show that increasing spatial resolution to 200 m could improve yields by two to three orders of magnitude, highlighting the importance of high-resolution observations for tropical greenhouse gas monitoring.

First, we evaluate the frequency and distribution of clear-sky data over tropical Africa for TROPOMI, the NIMCAM IOD, and a constellation of NIMCAM instruments, using high-resolution Sentinel-2 cloud probability data and downscaled MODIS aerosol optical depth data. We translate this information into gridded uncertainty estimates by co-adding data, assuming per-measurement random error estimates. Finally, using the GEOS-Chem model and an ensemble Kalman Filter (Feng et al., 2009), this information forms the basis of closed-loop numerical experiments that evaluate the ability of NIMCAM to quantify

https://doi.org/10.5194/egusphere-2026-812
Preprint. Discussion started: 23 February 2026

large-scale diffuse emissions of methane over tropical Africa, predominately originating from wetlands, and compare it against synthetic TROPOMI data that has observed the same scenes. We focus on the months corresponding to the short (March and April) and long rain (October and November) seasons over the region in 2019 for which previous studies revealed substantial methane pulses (Lunt et al., 2019, 2021; Shaw et al., 2022).

In the next section, we describe the data and methods we use to evaluate the ability of NIMCAM data and compare its performance against synthetic TROPOMI data. In section 3, we report our results for the clear-sky data distribution, co-addition of errors, and the corresponding methane emission estimates. We conclude the study in section 4.

2 Data and methods

2.1 The Near Infrared Multispectral Camera for Atmospheric Methane

NIMCAM is a new EO satellite mission concept that has been designed to address the science requirements associated with identifying and monitoring changes in atmospheric methane due to emissions from large point sources. It has been under development at the University of Edinburgh since 2017.

The core NIMCAM instrument is a multispectral imager, optimised for detecting changes in atmospheric methane at high spatial resolution and with global coverage (Woodwark et al., 2026). NIMCAM employs a novel design using a minimal number of spectral channels located near 1640 nm. Each channel features a very narrow bandpass width of 1.0 nm Full Width Half Maximum, with the channels positioned in close proximity to one another. The spectral design consists of an "on-band" channel located at a methane absorption feature, bracketed by two "off-band" channels which provide a fit for background spectral various and other confounding species. Modelling work based on this three-channel design has demonstrated good methane signal contrast and reliable rejection of confounding water and ground reflectance signals. Observing in the near infrared brings several benefits including a greater sensitivity to near-surface methane compared with thermal infrared observations and reduced requirements for detector and optical system cooling. Narrow bandpass interference filters define the spectral channels, manufactured by depositing thin layers of coatings over a substrate material.

Other aspects of the NIMCAM flight instrument design include a telescope with primary aperture of 135 mm, imaging a cross-track field of view of 2.9°. We use a commercial Indium Gallium Arsenide (InGaAs) detector from Raptor Photonic, which provides a resolution of 640×512 pixels. Manufacturer-provided detector specifications have been used during our modelling work to assess the Signal to Noise Ratio of the system. NIMCAM operates with a swath width of approximately 30 km, and 60 metre ground pixels. The narrow bandpass filters are arranged in strips across the field of view. As the scene moves under the instrument it sweeps across the filters, meaning a point on the ground is imaged through all channels during an overflight, providing the required channels of spectral data for each spatial pixel. Telecentric relay elements provide the necessary optical conditions to maintain filter spectral performance.

The instrument is nadir-viewing, and no additional tasking or targeting manoeuvres are required during flight, so that the orbital configuration delivers a weekly revisit interval for most land surface locations. NIMCAM's continuous observation approach means currently unknown or unsuspected leaks are more likely to be captured, driving a proactive rather than reactive

https://doi.org/10.5194/egusphere-2026-812
Preprint. Discussion started: 23 February 2026

approach to fugitive emission detection. The simplified spacecraft guidance and attitude control possible with a fixed nadir view also reduces cost and mission complexity.

2.2 NIMCAM in-orbit demonstrator and constellation mission concepts

NIMCAM is designed for deployment on a constellation of up to 9 small satellites in Sun Synchronous Low Earth Orbit at an altitude of approximately 600 km and orbital inclination of 97.8°. Each instrument provides a single-frame footprint of 38.4×30.7 km^2. In this study, we assess the capacbility of a single in-orbit demonstrator (IOD), compared to a constellation of three and five satellities. Each satellite follows an orbital ground track with a 10-day repeat cycle, giving close to full global coverage in 10 days with the five satellite configuration.

Our study area encompasses tropical Africa, spanning 10°S to 20°N between the mainland coasts (Fig.1). Fig. 1a and 1b display the NIMCAM IOD and constellation data coverage for a single day and a full 10-day cycle, respectively, while Fig. 1c provides the 10-day IOD coverage for comparison. We use these configurations to analyse clear-sky data availability for the IOD and the proposed three- and five-satellite constellations.

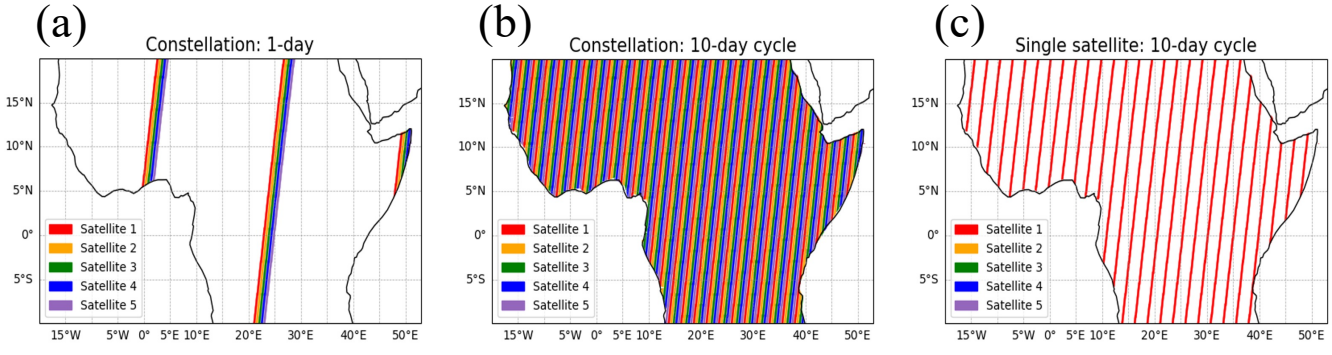

Figure 1. The ground track satellite coverage within our tropical African region: (a) the five-satellite NIMCAM constellation for the first day of the cycle, (b) the five-satellite NIMCAM constellation for the 10-day cycle, and (c) the in-orbit demonstrator NIMCAM concept for the 10-day cycle.

2.3 Sentinel 2 cloud probability data

We evaluated cloud interference using the Sentinel-2 cloud probability feature. Data retrieval was performed via the Google Earth Engine Python API (Gorelick et al., 2017). To maintain spatial consistency with our NIMCAM model, the 10 m data was resampled to 60 m, reprojected to the local UTM coordinate system, and exported in GeoTIFF format. We synchronised the temporal resolution with NIMCAM's 10-day repeat cycle, capturing three distinct data periods per month.

Cloud Probability (CP) is a common metric for quality masking in greenhouse gas retrievals. However, the literature reveals significant variation in established cutoff thresholds. For instance, Zhang et al. (2022) used a relaxed threshold for Sentinel-2

https://doi.org/10.5194/egusphere-2026-812
Preprint. Discussion started: 23 February 2026

methane retrievals, considering an area cloud-free if the CP was below 65% and filtering out scenes where more than 10% of the region exceeded this limit. In contrast, studies of GOSAT-2 CO_2 and CH_4 observations adopted a more stringent filter, excluding all data with a CP $>$ 10% (Suto et al., 2021). While reported limits in other studies span a broad range from 5% to 70% (Faruolo et al., 2023; Manninen et al., 2022; Declaro and Kanae, 2024), we have opted for a conservative 10% limit. This strict threshold reflects the high-quality control likely required for NIMCAM observations and allows us to evaluate the specific advantages of NIMCAM's high horizontal resolution when operating under challenging cloud conditions, as found over tropical ecosystems.

We sample cloud information at the Sentinel-2 local solar time of equatorial crossing (10:30 LST), which may introduce a diurnal bias. To estimate the impact of this bias, we performed an analysis on the GEOS-FP cloud fraction dataset, which provides cloud information at a coarser horizontal resolution of 0.25°x0.3125°, but at a higher temporal resolution of every three hours (Appendix, Fig. B1). Looking at cloud variability across the whole African region, cloud levels tend to be higher during the night, while during daylight hours they remain relatively stable. This suggests that cloud measurements taken at 10:30 LST do not exhibit a significant bias compared to other times of day. However, in the cloudiest region of tropical Africa, centred around the Congo Basin, there is a more distinct diurnal cycle during daylight hours. Cloud cover appears higher in the morning and evening, with a minimum occurring between 12:00 and 15:00 LST. In this region, cloud data extracted at 10:30 LST may slightly overestimate cloud levels at other times of day.

2.4 MODIS aerosol data

To characterise aerosol loading, we extract MODIS aerosol optical depth (AOD) in the green band (0.55 μm) at 1 km spatial resolution. Data were downloaded using the Earth Engine Python API in an analogous method to the cloud probability data extraction. MODIS has a 16-day repeat cycle, with additional data gaps due to quality screening. To maximise coverage, we aggregate the data over monthly periods. AOD is commonly used for quality masking in greenhouse gas retrieval studies, with thresholds typically ranging from 0.75 to 0.20 (Liu et al., 2024; Buchwitz et al., 2013; Li et al., 2022; Virtanen et al., 2024; Garrigues et al., 2022), and in some cases even more stringently with a threshold of 0.10 (Yu et al., 2024). For this study, we explore the more conservative thresholds, comparing the data availability for AOD cutoffs of 0.20 and 0.10. We downscale the 1 km MODIS AOD to the NIMCAM 60 m grid using a Gaussian probalistic approach, described in Appendix A.

2.5 Translating raw EO data onto GEOS-Chem grid for atmospheric inversion studies

The nested GEOS-Chem atmospheric chemistry and transport model (ACTM), described below, has a horizontal resolution of 0.25° (latitude) × 0.315° (longitude), which is coarser than the NIMCAM 60 m resolution. To assess the theoretical ability of NIMCAM to infer methane fluxes over tropical Africa, we count all available NIMCAM 60 m clear-sky scenes into the GEOS-Chem model grid boxes along the NIMCAM ground track swath. They form the basis of NIMCAM "super observations."

To determine clear-sky NIMCAM scenes, we use the 60 m Sentinel-2 cloud probability dataset, and the downscaled 60 m MODIS AOD dataset, described above. The available NIMCAM pixel count is determined for the condition: CP$<$10%, AOD$<$0.1. This translates to a NIMCAM dataset described on the GEOS-Chem modelling coordinate system, with the data

https://doi.org/10.5194/egusphere-2026-812
Preprint. Discussion started: 23 February 2026

availability at a temporal resolution of one hour. We use this approach for the NIMCAM IOD and NIMCAM constellations, as described above. Within each GEOS-Chem model grid, there are up to 270,000 NIMCAM 60 m pixels available. Data were prepared for GEOS-Chem model runs to perform methane flux inversions.

2.6 The GEOS-Chem Atmospheric Chemistry Transport Model (ACTM) and the Ensemble Kalman Filter (EnKF)

Methane inversion experiments are conducted for April and October 2019, corresponding to the long and short rain seasons over East Africa, respectively (Palmer et al., 2023). Synthetic methane observations are generated for the NIMCAM IOD and the three- and five-satellite constellations, and consistently for the TROPOMI instrument.

We use the GEOS-Chem ACTM to describe the relationship between surface emissions of methane and observed changes in atmospheric methane. We use the nested version of the GEOS-Chem ACTM (version 13.4) to describe atmospheric methane within our tropical Africa domain (38°S–38°N, 20°–55°E). The nested model uses a horizontal resolution of 0.25° (latitude) × 0.3125° (longitude) and is driven by the GEOS-FP meteorological analysis from the Global Modeling and Assimilation Office, based at NASA Goddard Space Flight Center (GSFC).

The prior simulations are forced by pre-defined anthropogenic and natural methane emission inventories, The natural methane fluxes include monthly wetland emissions covering rice paddies (Bloom et al., 2017); monthly fire emissions (van der Werf et al., 2017); and termite emissions (Fung et al., 1991). We also account for emissions from geological macroseeps (Kvenvolden and Rogers, 2005; Etiope, 2015). For anthropogenic emissions, we use the EDGAR v4.32 global emission inventory (Janssens-Maenhout et al., 2019), which includes a range of human-related sources such as the oil and gas sector, coal mining, livestock, and waste management. To represent the main oxidation sink of methane, we use monthly 3-D OH fields from the GEOS-Chem full-chemistry simulation (Mao et al., 2013; Turner et al., 2015), which are consistent with observed constraints on the lifetime of methyl chloroform.

The lateral boundary conditions are taken from a self-consistent global version of the ACTM but run on a coarser horizontal resolution of 2.0° (latitude) × 2.5° (longitude) using GEOS-FP meteorological reanalyses. This global model has been fitted to GOSAT proxy XCO2:XCH4 retrievals (Feng et al., 2023). We use the posterior fluxes over Africa, inferred from these GOSAT data, as the truth in our closed-loop experiments to describe NIMCAM dry-air column methane mole fraction retrievals (XCH4) in the GEOS-Chem ACTM. We assume that the prior flux estimates for the study region (10°S–20°N, 20°W–50°E) are the same as the prior inventories used by Feng et al. (2023). Our nested model region is larger than our study region to minimise the influence of lateral boundary conditions.

In the absence of real NIMCAM data, we use a closed-loop experimental configuration in which we define a "true" methane emission distribution that is used to determine the "true" 4-D distribution of atmospheric methane. We then sample that 4-D field as it would be observed by NIMCAM, considering its orbit, across-track measurement strategy, and the instrument averaging kernel that describe the instrument vertical sensitivity to changes in atmospheric methane (Appendix B2), and remove observed scenes according to CP<10% and AOD<0.1. We add realistic sources of instrument noise to these NIMCAM "observations", with a simple error model of 15 ppb for solar zenith angles (SZA) below 40° and 30 ppb for SZA above 40°, comparable to the true GOSAT observational uncertainty. We then use these "observations" to infer posterior methane emission

https://doi.org/10.5194/egusphere-2026-812
Preprint. Discussion started: 23 February 2026

estimates using the GEOS-Chem ACTM, driven by a different methane emission distribution and an EnKF. For comparison, we use a similar approach to generate synthetic TROPOMI observations. The locations for the quality-filtered (qa>0.75) TROPOMI data are taken from an operational L2 XCH_4 product (Schneising et al., 2019, 2023).

We anticipate it is likely there will be many 60 m NIMCAM observations that fall within each GEOS-Chem nested model grid. In our closed-loop experiments, we assimilate only one "super observation" for each model grid. To achieve this, we sample the GEOS-Chem model fields for each grid containing clear-sky NIMCAM observations (Section 3.1) and calculate individual values of XCH_4. This is done by convolving the resulting model methane profiles with an averaging kernel. The averaging kernels for NIMCAM are not fully characterised, so we assume values from GOSAT that vary with solar zenith angle and surface type. We assume the observation uncertainty δ for the NIMCAM super observations is described by:

$$\delta = \delta_l + \frac{\delta_{GOSAT}}{\sqrt{N}}, \tag{1}$$

where δ_l is the uncertainty lower limit, which describes sub-grid variations and scene-dependent biases, and N is the number of clean observations over land. The value of N is calculated by multiplying the number of NIMCAM clear-sky observations that fall within a grid's land fraction.

To infer posterior methane emission estimates from these atmospheric data, we use a modified version of Local Ensemble Transform Kalman Filter (LETKF) (Scarpelli et al., 2024). We use an ensemble of 91 flux perturbations at the model grid to represent the methane flux uncertainty over our study region. The prior uncertainty of methane fluxes is still challenging to quantify, with natural emissions often misallocated or even missing at the model grid resolution. Here, for simplicity, we define the prior uncertainty of the methane emission at each grid box by:

$$\sigma = 0.2(S_{prior} + [S_{prior} - S_{posterior}]), \tag{2}$$

where S_{prior} and S_{post} denote the prior posterior emission estimate, respectively, from the corresponding global inversion (Feng et al., 2022). We assume the error correlation between grid boxes is 100 km, following previous studies (Scarpelli et al., 2024; Kurganskiy et al., 2025). The posterior uncertainty is given by:

$$S_{post} = \left(S_{prior}^{-1} + K S_{obs}^{-1} K^T\right)^{-1}, \tag{3}$$

where S_obs denotes the observational error covariance matrix, K denotes the Jacobian that describes the sensitivity of the observation (in this case, NIMCAM methane columns) to changes in surface emissions of methane.

We calculate the uncertainty reduction, to assess the theoretical potential of NIMCAM data, expressed as a percentage:

$$\eta = \sqrt{\left(1 - \frac{S_{post}^{ii}}{S_{prior}^{ii}}\right)} \cdot 100, \tag{4}$$

where S_x^{ii} denotes the i^{th} diagonal elements of the error covariance matrix.

https://doi.org/10.5194/egusphere-2026-812
Preprint. Discussion started: 23 February 2026

3 Results

Here, we report all-sky and clear-sky data coverage statistics for the NIMCAM IOD and its constellation concepts and compare them against the performance of TROPOMI for the same synthetic atmosphere. We compare the co-added uncertainties associated with these NIMCAM and TROPOMI datasets after they are gridded onto the nested GEOS-Chem model grid. Finally, using a series of closed-loop numerical experiments, we examine the ability of these instruments to estimate "true" methane emission estimates.

3.1 All-sky data coverage statistics

We evaluate the data availability of NIMCAM methane observations (60 m resolution, 10-day repeat cycle) under three scenarios: as an IOD and as part of three- and five-satellite constellations. To provide context, these results were compared against the all-sky distribution of 7 km resolution data (equivalent to TROPOMI) and a 1 km resolution retrieval with a 5-day repeat cycle (equivalent to GOSAT-2).

First, we consider all-sky methane retrievals aggregated onto 7 km grid cells with a temporal resolution of 10 days, corresponding to the approximate repeat time of the NIMCAM IOD. The number of potential NIMCAM retrievals is affected by the image resolution and the temporal resolution. For NIMCAM, the IOD only provides coverage of 19% of the region over the 10-day period, while the three and five satellite constellations achieve 54% and 89% coverage, respectively (Fig. 2). In comparison, TROPOMI provides 100% coverage daily due to its significantly larger across-track swath of 2,600 km. In other words, daily TROPOMI all-sky coverage is comparable to 10 days of NIMCAM data collected by the five-constellation mission concept. At the 1 km resolution, we implement a 5-day repeat cycle, which translates to all-sky coverage every 5 days, and therefore 2 observations within each 10-day cycle.

Within each 7 km grid cell, there are 13,611 NIMCAM pixels at 60 m resolution, 49 pixels at 1 km resolution (nominally GOSAT-2), and a single pixel at 7 km resolution (nominally TROPOMI). However, the more frequent revisit times of GOSAT-2 and TROPOMI data means that the number of retrievals per 10-day cycle increases to 98 and 10 for the 1 km and 7 km resolution scenarios, respectively.

3.2 Clear-sky data coverage statistics

We now consider how cloud and aerosols affect the data availability at the different instrument retrieval spatial resolutions. Fig. 3 shows the proportion of 7 km grid cells within our tropical African study region that are affected by cloud cover and elevated AOD (values of 0.1 and 0.2, as described above) for the four months of our study.

October is the cloudiest month corresponding to the short rains season, with an average cloud coverage of 77%. Most of the cloud cover is over the southern and mid-latitude areas including the tropical rainforest regions (Congo Basin, Guinean forests of West Africa, and eastern Afromontane). The cloud coverage is slightly lower for March, April, and November with an average coverage of 57%, 62% and 60%, respectively. Distributions of AOD loading over the regions are are primarily influenced by seasonal biomass burning. Using an AOD threshold of 0.2, March exhibits the highest fraction of affected

https://doi.org/10.5194/egusphere-2026-812
Preprint. Discussion started: 23 February 2026

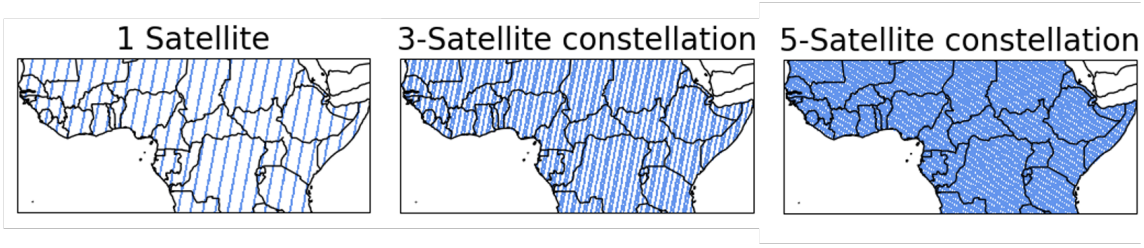

Figure 2. Number of all-sky NIMCAM passes within each 7 km grid cell across the region during a 10-day cycle for the IOD and the three- and five-satellite constellation mission concepts. Coverage is defined as the proportion of 7 km grid cells with at least one satellite pass over the 10-day period. The IOD covers 18% of grid cells, while the three- and five-satellite constellations increase coverage to 54% and 89%, respectively.

pixels (55%), followed by April (44%), October (37%), and November (19%). Using a stricter AOD threshold of 0.1, the corresponding values increase substantially, with March at 94%, April at 90%, October at 87%, and November at 80%. These results reflect the known seasonal cycle of biomass burning over Central and West Africa, which peaks during the late dry season in March–April and is lowest in November.

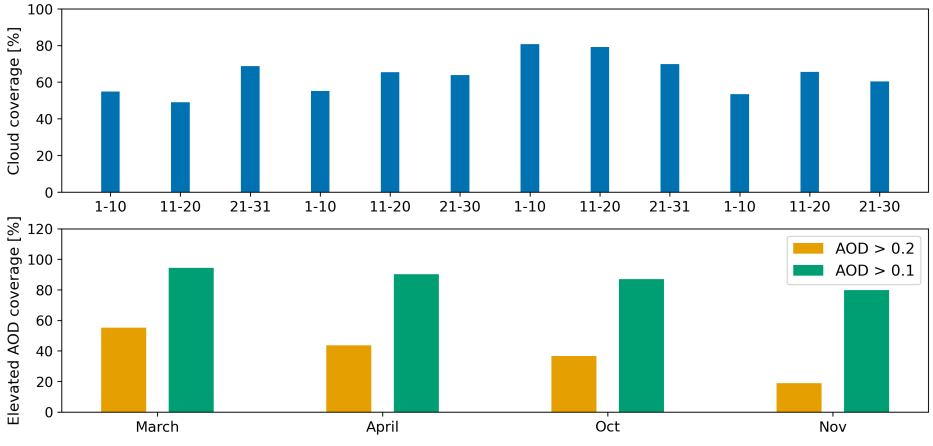

Figure 3. Monthly cloud coverage (top) and elevated AOD coverage (bottom) across our study region (10°S to 20°N, mainland Africa) for March, April, October, and November, 2019. Elevated AOD is shown for thresholds of 0.2 and 0.1.

Fig. 4 shows the spatial distribution of data availability following cloud masking (CP > 10%) alone, and combined cloud and aerosol masking using AOD thresholds of 0.2 and 0.1. All scenarios are evaluated on a common 7 km analysis grid, and data availability is quantified as the total number of clear-sky retrieval pixels accumulated within each 7 km cell over a 10-day observation window. We present results for April and October 2019 (with March and November shown in Appendix B3) for the NIMCAM IOD, and the 3- and 5-satellite NIMCAM constellations. NIMCAM observations are simulated at their native

https://doi.org/10.5194/egusphere-2026-812
Preprint. Discussion started: 23 February 2026

60 m resolution and aggregated to the 7 km grid. For comparison, we also include a 1 km resolution, 5-day repeat scenario (nominally GOSAT-2) and a 7 km resolution, daily repeat scenario (nominally TROPOMI).

Looking at cloud masking alone, the NIMCAM IOD (single satellite) achieves the lowest fractional coverage, ranging from 10–15% of the domain, as expected, reflecting its limited swath – in a clear-sky scenario the IOD only cover 18% of the region. Three NIMCAM satellites improve coverage, while five NIMCAM satellites consistently surpass the TROPOMI scenario, and generally match or slightly underperform the GOSAT-2 scenario. Across all months, NIMCAM's high native spatial resolution of 60 m leads to 2–3 orders of magnitude more clear-sky pixels per 7 km cell compared to the TROPOMI and GOSAT-2 scenarios, as shown by the colour bar of monthly counts.

The benefits of NIMCAM's finer resolution are most evident in October, the cloudiest month. Here, three NIMCAMs outperform the TROPOMI scenario, and five NIMCAMs achieve comparable coverage to the GOSAT-2 scenario, despite the overall lower fractional coverage of the domain. Elevated cloud cover at TROPOMI resolution obscures almost the entirety of the African tropical rainforest regions, while NIMCAM's finer sampling spreads observations across a wider area of cells, reducing contiguous gaps and providing more spatially distributed information.

When additionally removing scenes with elevated AOD, data availability declines further, with the largest impacts observed in March and April and primarily affecting the northwest of the domain. At the moderate AOD threshold of 0.2, the NIMCAM IOD still shows the lowest coverage across all months, while three NIMCAM satellites surpass the TROPOMI scenario in every month except November. Additionally, the five-satellite NIMCAM constellation consistently outperforms the GOSAT-2 5-day repeat scenario in all months except November.

Applying the stricter AOD threshold of 0.1 leads to a dramatic reduction in data availability for the TROPOMI scenario, with clear-sky coverage dropping to 4% of the domain in March, April, and October, and 14% in November. Under these conditions, NIMCAM's high-resolution observations become increasingly valuable. The single NIMCAM satellite now outperforms the TROPOMI scenario in all months except November, although its valid 7 km cells are more widely distributed across the domain, whereas the TROPOMI retains coverage primarily in the most northern areas. Three NIMCAM satellites exceed both the GOSAT and TROPOMI scenarios in all months, including November, while the full five-satellite constellation achieves the highest coverage overall: April, 39%; October, 42%; March, 27%; and November, 58%.

These results demonstrate that the finer 60 m resolution of NIMCAM leads to a substantially more spatially extensive and distributed dataset, especially when clouds and aerosols remove large fractions of coarser-grid pixels. As data masking becomes stricter, the advantages of NIMCAM's high resolution and multi-satellite configurations become increasingly pronounced. O

To evaluate the use of these satellite data for methane flux inversions (e.g. using GEOS-Chem and the ensemble Kalman filter, section 3.4), we calculate the number of GEOS-Chem nested model grid boxes ($0.25° \times 0.3125°$) containing clear-sky observations for each 10-day study period. We compared the data density of TROPOMI against the NIMCAM IOD and the three-satellite and five-satellite constellations (Figure 5). We find there are more observations for TROPOMI than the single NIMCAM IOD when we mask for clouds and use a AOD threshold of 0.2. However, when we adopt a stricter AOD threshold of 0.1 with the cloud masking, the NIMCAM IOD coverage exceeds TROPOMI across every 10-day period. The three-satellite and five-satellite NIMCAM constellations consistently outperform TROPOMI in grid-box availability. This relative advantage

https://doi.org/10.5194/egusphere-2026-812
Preprint. Discussion started: 23 February 2026

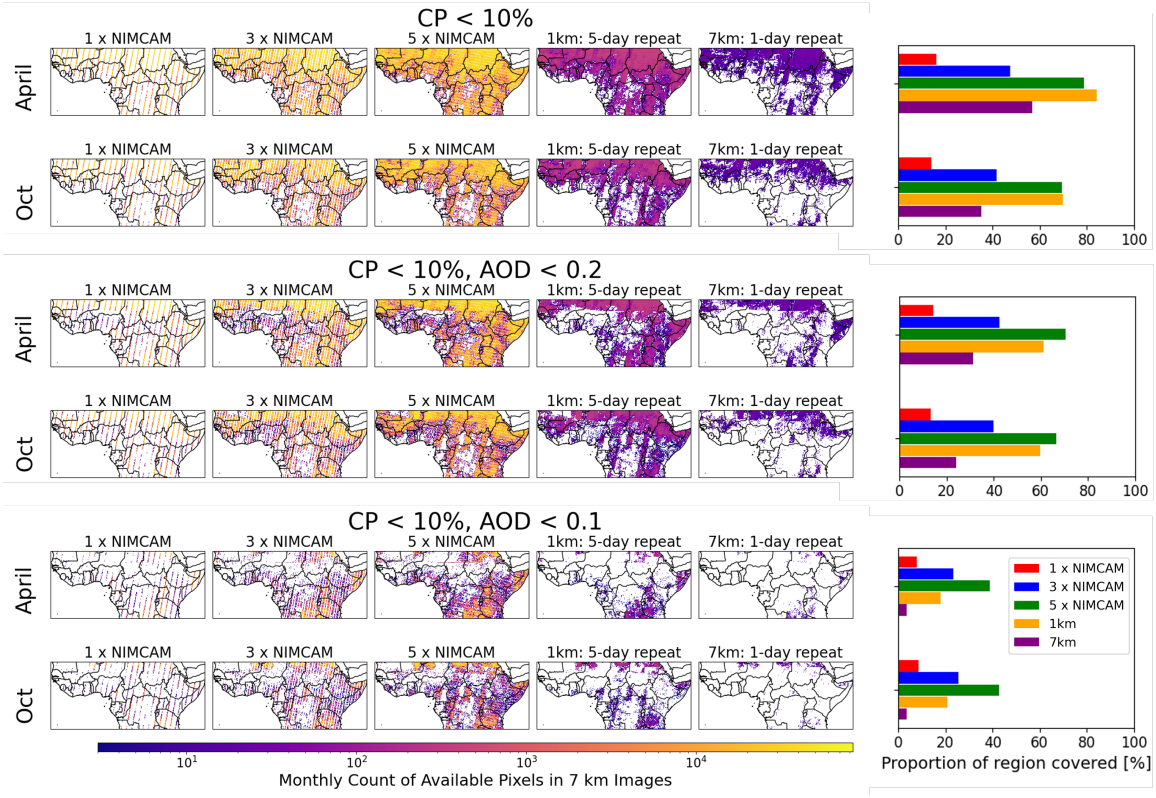

Figure 4. Total number of clear-sky retrieval pixels accumulated within each 7 km grid cell over a 10-day observation window for April and October. Results are shown for the NIMCAM IOD and the three- and five-satellite constellation mission concepts, a 1 km retrieval (5-day repeat, nominally GOSAT-2), and a 7 km retrieval (daily repeat, nominally TROPOMI). Compared for cloud masking (CP<10%) and AOD masking (thresholds 0.2 and 0.1). Bar charts indicate the proportion of 7 km grid cells with available data.

becomes more pronounced as the AOD masking criteria become more stringent. Using the 5-satellite constellation and our strict 0.1 AOD/cloud mask, NIMCAM provides up to 6 times more valid grid boxes than TROPOMI. These results demonstrate that NIMCAM's higher spatial resolution significantly enhances data availability, particularly in regions where strict quality filtering would otherwise limit observational coverage.

3.3 Improving the signal to noise of super observations of co-adding NIMCAM data

Here, we investigate how higher spatial resolution data influences random errors in accumulated methane super-observations on the GEOS-Chem nested model resolution of $0.25° \times 0.3125°$. By comparing TROPOMI precision with estimated NIMCAM retrieval errors, mapped to the nested GEOS-Chem model grid over 10-day intervals, we quantify the impact of data co-addition. Under the assumption of uncorrelated noise, the random error scales by $1/\sqrt{N}$, where N is the number of pixels contributing to each super-observation.

https://doi.org/10.5194/egusphere-2026-812
Preprint. Discussion started: 23 February 2026

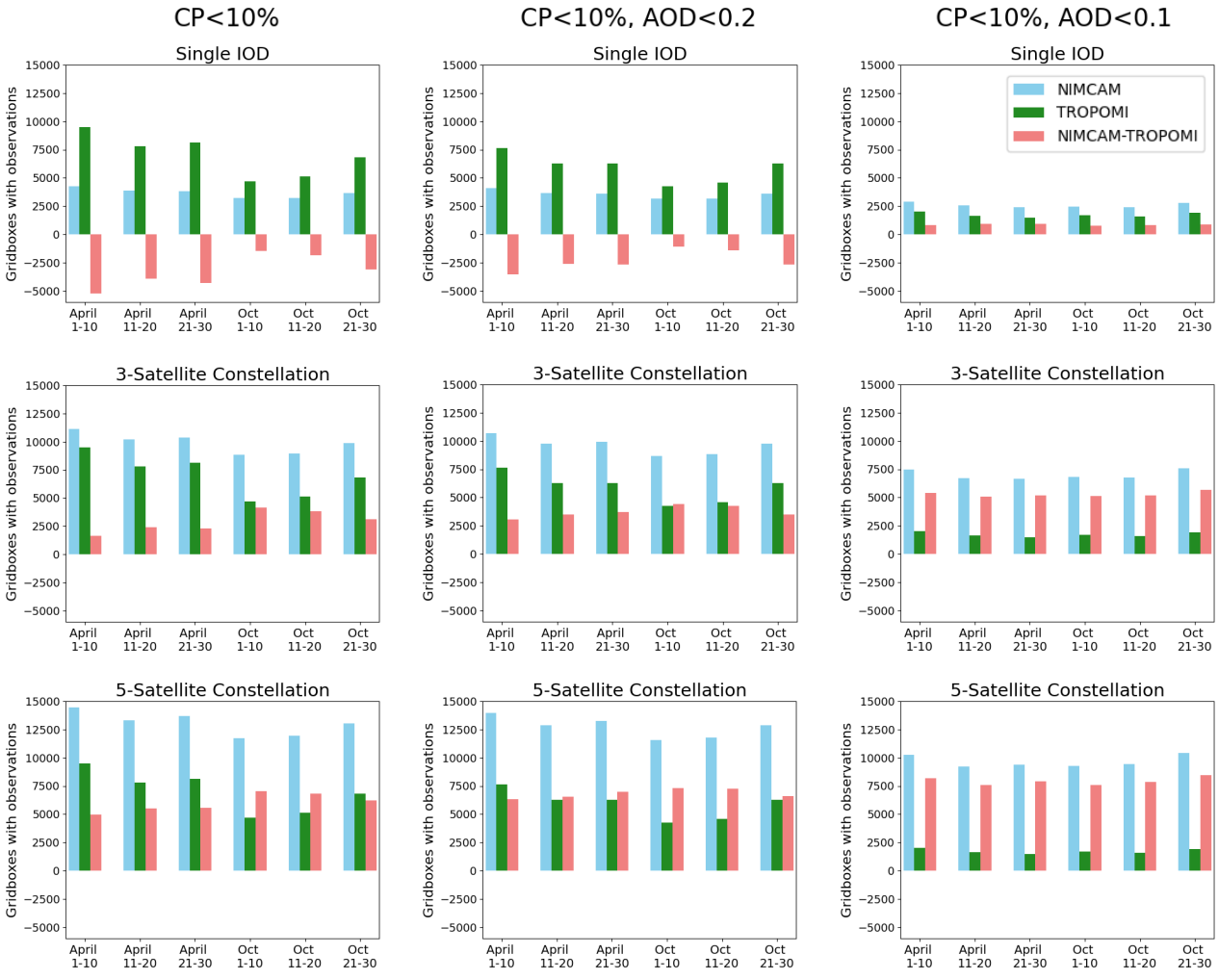

Figure 5. The number of GEOS-Chem nested model $0.25^\circ \times 0.3125^\circ$ grid boxes with available observations compared between NIMCAM (blue) and TROPOMI (green) and the difference (NIMCAM minus TROPOMI, red). Plotted for the 6, 10-day cycles through April, and October. Shown for a single NIMCAM IOD (top panel), a three-satellite constellation (middle panel), and the full five-satellite constellation (bottom panel). Compared when masking just for cloud (left panel), as well as cloud and AOD at 0.2 (middle panel) and AOD at 0.1 (right panel).

Analysis of TROPOMI CH_4 column data reveals an average single-pixel precision of $(2.5 \pm 1.0) \times 10^{15}\,\mathrm{molec\,cm^{-2}}$. The NIMCAM single-pixel random error is estimated to be $2.5 \times 10^{17}\,\mathrm{molec\,cm^{-2}}$, based on radiative transfer simulations and retrieval algorithm modelling (Woodwark et al., 2026). Although this is two orders of magnitude worse than TROPOMI at the single-pixel level, commensurate with the different science requirements, it is achieved at a substantially finer spatial resolution. The native NIMCAM pixel size is approximately 117 times smaller in linear dimension than TROPOMI, implying

https://doi.org/10.5194/egusphere-2026-812
Preprint. Discussion started: 23 February 2026

that a single TROPOMI footprint contains roughly 13,689 NIMCAM pixels. Conversely, TROPOMI provides approximately ten times higher temporal sampling than NIMCAM.

When aggregated to our GEOS-Chem nested model resolution of $0.25° \times 0.3125°$ over a 10-day window, the maximum potential sample size for NIMCAM reaches 273,780 pixels (468×585), whereas TROPOMI yields at most ∼200 measurements (10 days × ∼20 pixels per day). The effective number of contributing pixels is further reduced by orbital coverage, such that the IOD, three-satellite, and five-satellite constellations sample approximately 18%, 54%, and 89% of the grid, respectively.

These results are summarized in Table 1. Under ideal clear-sky conditions, the ratio of random error in NIMCAM super-observations to that of TROPOMI super-observations ($\sigma_{\mathrm{NIM}}/\sigma_{\mathrm{TROP}}$) is 6.1, 3.6, and 2.8 for the IOD, three-satellite, and five-satellite constellations, respectively. This ratio metric is used in the following sections to assess how relative performance evolves under cloud and aerosol masking.

		Per pixel σ [molec cm^{-2}]	N	Super Observation σ [molec cm^{-2}]
NIMCAM	IOD	2.5×10^{17}	49,280	1.1×10^{15}
	three-Satellite	2.5×10^{17}	147,841	6.5×10^{14}
	five-Satellite	2.5×10^{17}	243,664	5.1×10^{14}
TROPOMI		2.5×10^{15}	200	1.8×10^{14}

Table 1. A clear-sky comparison between NIMCAM (IOD, three-satellite, five-satellite) and TROPOMI, showing the average per-pixel error of retrievals, the number of potential observations per GEOS-Chem grid box in 10 days (N), and the corresponding error of the co-added super-observations.

Figure 6 illustrates how the ratio between NIMCAM and TROPOMI super-observation random errors changes when progressively masking for clouds and aerosols. Across all scenarios, data masking leads to a proportionally larger increase in TROPOMI error relative to NIMCAM, such that the majority of grid cells exhibit error ratios lower than the corresponding clear-sky value. This effect is most pronounced for the single-satellite IOD case, for which the 75th percentile of the error ratio distribution lies well below the clear-sky reference. This indicates that, despite its more limited spatial coverage, a single NIMCAM platform can still generate methane super-observations with random errors that are, in most cases, comparable to those achieved by the three- and five-satellite constellations under realistic filtering conditions.

Including AOD filtering in addition to cloud masking further enhances the relative advantage of NIMCAM, with the error ratio decreasing under AOD masking and showing additional reductions when applying the stricter AOD threshold of 0.1. Both the magnitude of the ratios and their overall trends are consistent between April and October, indicating that the behaviour is robust across seasons. Overall, these results demonstrate that high-resolution NIMCAM measurements are more resilient to data loss than TROPOMI. As cloud and aerosol filtering become increasingly stringent, NIMCAM exhibits a smaller relative degradation in effective sampling, leading to a slower growth in super-observation random error.

https://doi.org/10.5194/egusphere-2026-812
Preprint. Discussion started: 23 February 2026

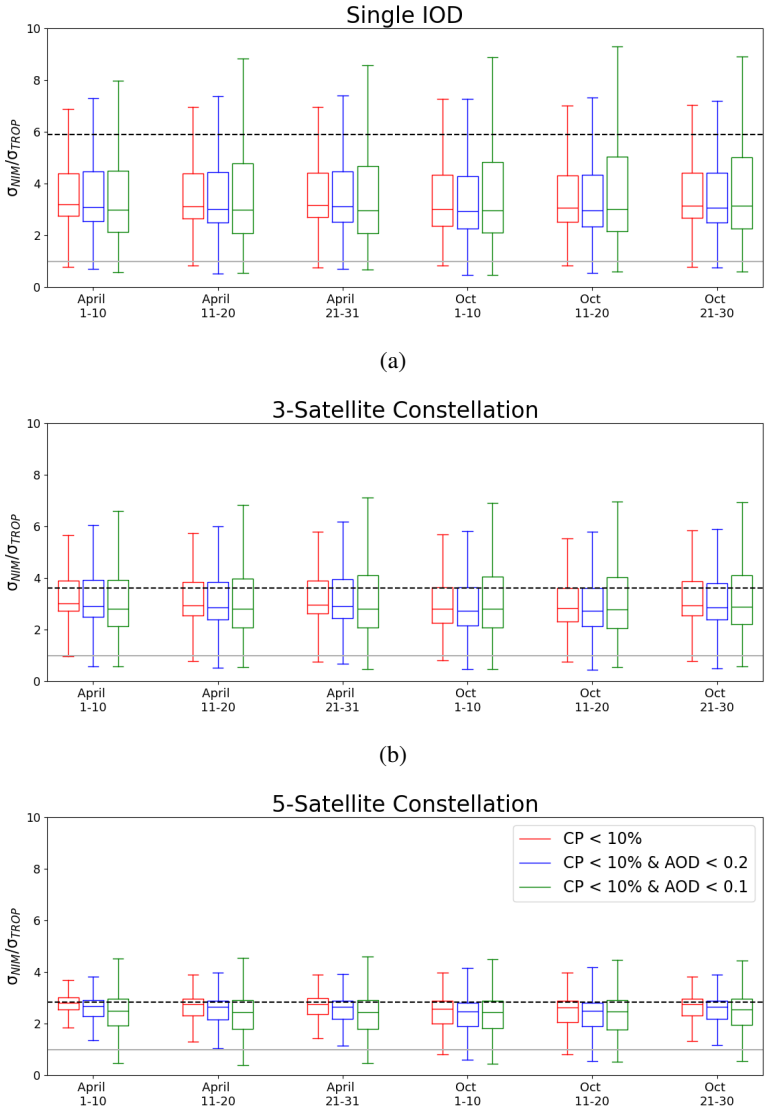

(a)

(b)

(c)

Figure 6. Statistical analysis of methane retrieval errors aggregated over a GEOS-Chem grid ($0.25^\circ \times 0.3125^\circ$) for 10-day intervals in April and October. Boxplots represent the NIMCAM/TROPOMI error ratio corresponding to cloud masking (red), and combined with AOD masking using thresholds of 0.2 (blue) and 0.1 (green). Presented for (a) Single satellite IOD, (b) the three-satellite constellation, and (c) the five-satellite constellation. Errors are modelled to scale by $1/\sqrt{N}$, where N denotes the count of valid observations. The dashed horizontal lines in panels (a), (b), and (c) denote the baseline ratio of 6.1, 3.6, and 2.8, respectively, when all data are available.

https://doi.org/10.5194/egusphere-2026-812
Preprint. Discussion started: 23 February 2026

3.4 Estimating regional methane emissions using synthetic NIMCAM and TROPOMI data

Fig. 7 show emission inversion estimates using simulated clear-sky observations of the NIMCAM IOD, the three and five NIMCAM constellation mission concepts, and TROPOMI for April 2019, respectively.

Compared to TROPOMI, the NIMCAM IOD shows data coverage across the study region instead of being focused over the broader Sahel region and Western Africa. The NIMCAM constellation fills in the observational gaps left by the IOD, with progressively more coverage over key methane-emitting regions, e.g. Congo Basin and the Sudd wetland regions in South Sudan. The biggest differences between the true values of XCH4 and values corresponding to prior knowledge are typically over the Congo Basin for the NIMCAM IOD and the constellations.

While XCH4 differences for NIMCAM mission concepts are generally larger than those for TROPOMI, reflecting the larger retrieval random errors for NIMCAM, the density of NIMCAM super-observations provides a distinct advantage. In key regions where TROPOMI clear-sky data are sparse, the high volume of NIMCAM data significantly reduces the discrepancy between the posterior and the true emission estimates. Consequently, NIMCAM demonstrates significant theoretical potential to constrain methane emission estimates over tropical Africa during the rainy season, effectively filling critical observational gaps left by TROPOMI.

Fig. 7b shows the corresponding improvements in the methane emission estimates in April. As expected, the posterior emission estimates are closer to the true values than the prior values. The NIMCAM IOD provides improvements for many of the key methane emitting regions, with progressive improvement with an increasing number of NIMCAM satellite in the constellation. The NIMCAM IOD outperforms TROPOMI for this month due to its ability to observe methane between clouds and elevated aerosol across the study domain. As a result, the uncertainty reduction, η, of these posterior emission estimates is generally larger for NIMCAM than for TROPOMI. We find that values of η begin to plateau with the three NIMCAM constellation – additional members of a constellation add valuable data but the measurement uncertainty begins to be small compared to errors associated with the atmospheric transport model. In other words, our ability to interpret these data is limited by the atmospheric transport model and not the data themselves.

Fig. 8 shows the same analysis but for October 2019 during the short rains across East Africa. Performance of NIMCAM is worse for this month due to more extensive cloud cover across the study region compared to April (Fig. 3). Similarly, the performance of TROPOMI is also worse for this month. After the NIMCAM data are ingested by the EnKF, we find that posterior estimate is much closer to the observations with substantial reductions over the Congo Basin. Unlike April, we find less evidence of the performance of the NIMCAM constellation plateauing after three satellites. This is because there are generally fewer clear-sky scenes, so the additional satellites are still providing valuable information to refine the methane emission estimates. This point is less obvious when we examine the posterior methane emission estimates but nevertheless the posterior solution is closer to the truth and the error reductions are larger. Much like April, additional satellites do not fill in the measurement gaps. To achieve that, the orbits would need to be further spread apart.

https://doi.org/10.5194/egusphere-2026-812
Preprint. Discussion started: 23 February 2026

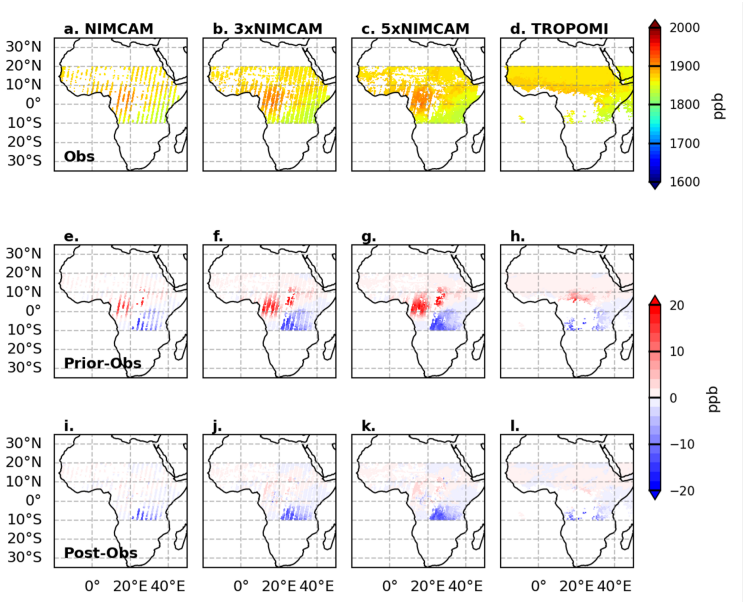

(a)

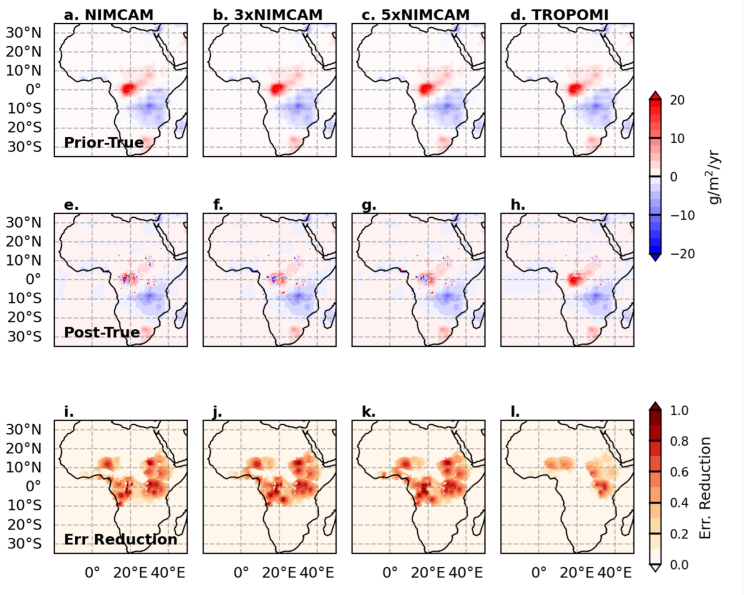

(b)

Figure 7. Synthetic methane emission inversion results for April 2019. a) Simulated clear-sky XCH_4 observations for the NIMCAM IOD, three- and five-satellite NIMCAM constellations, and TROPOMI (top), with residuals relative to the prior (middle) and posterior (bottom). (b) Prior emission bias relative to the truth (top), posterior emission residuals (middle), and inversion error reduction (bottom).

https://doi.org/10.5194/egusphere-2026-812
Preprint. Discussion started: 23 February 2026

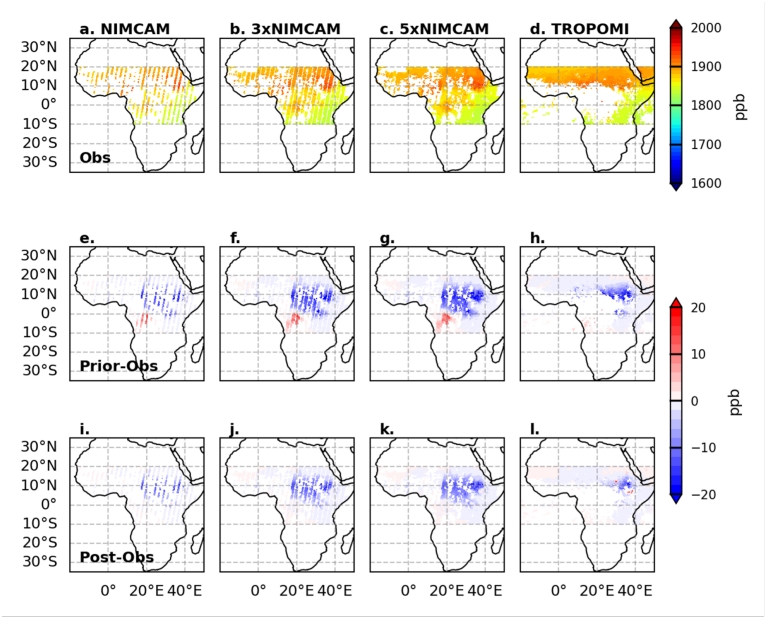

(a)

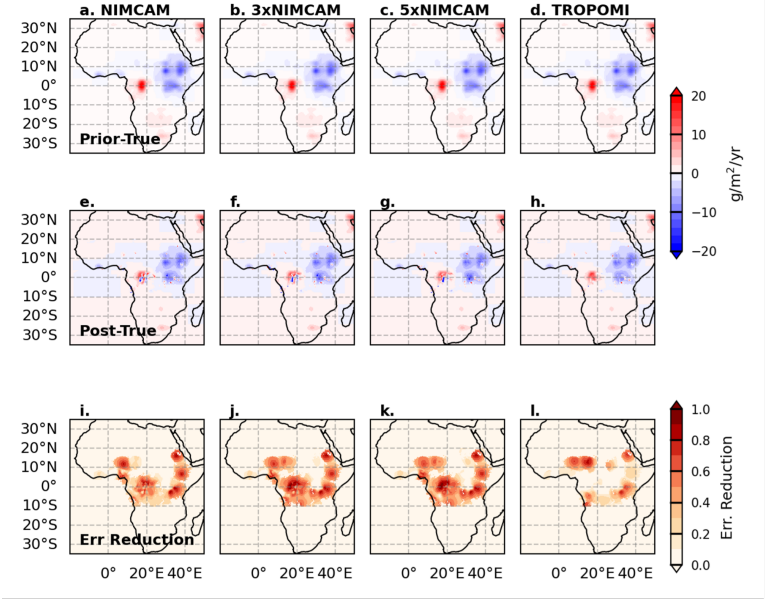

(b)

Figure 8. As Fig. 7 but for October 2019.

https://doi.org/10.5194/egusphere-2026-812
Preprint. Discussion started: 23 February 2026

4 Concluding remarks

The results of this study underscore the unique capability of NIMCAM to bridge significant observational gaps in tropical methane monitoring. By using a high spatial resolution of approximately 60 metres, NIMCAM can effectively view between fragmented cloud cover and regions of elevated aerosol optical depth that frequently obscure coarser area mappers like TROPOMI and GOSAT. In persistently cloudy regions such as the Congo Basin, where the kilometre-scale pixels of traditional sensors are often contaminated, NIMCAM's ability to retrieve clear-sky data between clouds ensures a more continuous and reliable record of wetland emissions.

While the signal-to-noise ratio of individual NIMCAM retrievals are significantly lower than that of larger flagship instruments, the high volume of clear-sky data points collected during peak emission seasons provides a robust statistical foundation for flux estimation. Our findings suggest that even conservative methane emission calculations derived from NIMCAM data offer substantial value, particularly in identifying diffuse sources within complex tropical ecosystems. The success of the NIMCAM In-Orbit Demonstrator further validates the mission concept and highlights the added value that a full constellation could provide in terms of temporal revisit frequency and global coverage.

More broadly, our study demonstrates the critical role that point source imagers play in the evolving global greenhouse gas observing system. As the field moves toward integrated multi-tiered architectures, the synergy between high-precision area mappers and high-resolution point source imagers will be essential for closing the methane budget. By providing the granular detail necessary to see between fragmented clouds and regions of elevated aerosol, instruments like NIMCAM, and the wider class of high-resolution satellite constellations, offer a scalable path to accurately quantify methane emissions from one of the world's most climate-critical regions.

5 Code/Data availability

The community-led GEOS-Chem model of atmospheric chemistry and transport is maintained centrally by Harvard University (https://geoschem.github.io/, last access: 10 Feb 2026) and is available on request. The ensemble Kalman filter code is publicly available as PyOSSE (https://www.nceo.ac.uk/data-facilities/datasets-tools//?dataset_type=tools, NCEO, last access: 10 Feb 2026).

6 Author Contributions

C.N.S. and P.I.P. designed the research; C.N.S., L.F., and A.J.P.W. prepared the calculations; C.N.S., L.F., and P.I.P. analysed the results; and C.N.S. and P.I.P. wrote the paper with contributions from L.F. and A.J.P.W.

7 Competing Interests

The authors declare that they have no conflict of interest.

https://doi.org/10.5194/egusphere-2026-812
Preprint. Discussion started: 23 February 2026

8 Acknowledgements

We gratefully acknowledge the GEOS-Chem community, particularly the team at Harvard University who help to maintain the GEOS-Chem model and the NASA Global Modeling and Assimilation Office (GMAO) that provided the MERRA2 data product.

9 Financial support

This study was funded by the Centre for Earth Observation Instrumentation (CEOI) through their 16th Funding Call, as part of the Flagship project “The Near Infrared Camera for Atmospheric Methane (NIMCAM): Instrument demonstration and space mission development," contract #RP10G0435A501. L.F. and P.I.P. were also funded by the NERC National Centre for Earth Observation (grant no. NE/R016518/1).

https://doi.org/10.5194/egusphere-2026-812
Preprint. Discussion started: 23 February 2026

References

Balasus, N., Jacob, D. J., Lorente, A., Maasakkers, J. D., Parker, R. J., Boesch, H., Chen, Z., Kelp, M. M., Nesser, H., and Varon, D. J.: A blended TROPOMI+ GOSAT satellite data product for atmospheric methane using machine learning to correct retrieval biases, Atmospheric Measurement Techniques, 16, 3787–3807, 2023.

Bloom, A. A., Bowman, K. W., Lee, M., Turner, A. J., Schroeder, R., Worden, J. R., Weidner, R., McDonald, K. C., and Jacob, D. J.: A global wetland methane emissions and uncertainty dataset for atmospheric chemical transport models (WetCHARTs version 1.0), Geoscientific Model Development, 10, 2141–2156, https://doi.org/10.5194/gmd-10-2141-2017, 2017.

Buchwitz, M., Reuter, M., Bovensmann, H., Pillai, D., Heymann, J., Schneising, O., Rozanov, V., Krings, T., Burrows, J., Boesch, H., et al.: Carbon Monitoring Satellite (CarbonSat): Assessment of atmospheric CO 2 and CH 4 retrieval errors by error parameterization, Atmospheric Measurement Techniques, 6, 3477–3500, 2013.

Bullock, E. L., Healey, S. P., Yang, Z., Oduor, P., Gorelick, N., Omondi, S., Ouko, E., and Cohen, W. B.: Three decades of land cover change in East Africa, Land, 10, 150, 2021.

Campbell, A., Potyk, L., and Poulter, B.: Modelling wetland methane emission estimates by leveraging new observations of anthropogenic point-source plumes, EGUsphere, 2025, 1–19, https://doi.org/10.5194/egusphere-2025-5398, 2025.

Charuvil Asokan, H., Landgraf, J., Veefkind, P., Dellaert, S., and Butz, A.: Assessing the detection potential of targeting satellites for global greenhouse gas monitoring: insights from TANGO orbit simulations, Atmospheric Measurement Techniques, 18, 5247–5264, https://doi.org/10.5194/amt-18-5247-2025, 2025.

Ciais, P., Zhu, Y., Cai, Y., Lan, X., Michel, S. E., Zheng, B., Zhao, Y., Hauglustaine, D. A., Lin, X., Zhang, Y., Sun, S., Tian, X., Zhao, M., Wang, Y., Chang, J., Dou, X., Liu, Z., Andrew, R., Quinn, C. A., Poulter, B., Ouyang, Z., Yuan, W., Yuan, K., Zhu, Q., Li, F., Pan, N., Tian, H., Yu, X., Rocher-Ros, G., Johnson, M. S., Li, M., Li, M., Feng, D., Raymond, P., Yang, X., Canadell, J. G., Jackson, R. B., Yu, X., Li, Y., Saunois, M., Bousquet, P., and Peng, S.: Why methane surged in the atmosphere during the early 2020s, Science, 391, https://doi.org/10.1126/science.adx8262, 2026.

Declaro, A. and Kanae, S.: Enhancing Surface Water Monitoring through Multi-Satellite Data-Fusion of Landsat-8/9, Sentinel-2, and Sentinel-1 SAR, Remote Sensing, 16, 3329, https://doi.org/10.3390/rs16173329, 2024.

Etiope, G.: Natural gas seepage, The Earth's hydrocarbon degassing, 199, 2015.

Faruolo, M., Genzano, N., Marchese, F., and Pergola, N.: Multi-Temporal Satellite Investigation of gas Flaring in Iraq and Iran: The DAFI Porting on Collection 2 Landsat 8/9 and Sentinel 2A/B, Sensors, 23, 5734, https://doi.org/10.3390/s23125734, 2023.

Feng, L., Palmer, P. I., Bösch, H., and Dance, S.: Estimating surface CO_2 fluxes from space-borne CO_2 dry air mole fraction observations using an ensemble Kalman Filter, Atmospheric Chemistry and Physics, 9, 2619–2633, https://doi.org/10.5194/acp-9-2619-2009, 2009.

Feng, L., Palmer, P. I., Zhu, S., Parker, R. J., and Liu, Y.: Tropical methane emissions explain large fraction of recent changes in global atmospheric methane growth rate, Nature Communications, 13, https://doi.org/10.1038/s41467-022-28989-z, 2022.

Feng, L., Palmer, P. I., Parker, R. J., Lunt, M. F., and Bösch, H.: Methane emissions are predominantly responsible for record-breaking atmospheric methane growth rates in 2020 and 2021, Atmospheric Chemistry and Physics, 23, 4863–4880, https://doi.org/10.5194/acp-23-4863-2023, 2023.

Frankenberg, C., Bar-On, Y. M., Yin, Y., Wennberg, P. O., Jacob, D. J., and Michalak, A. M.: Data Drought in the Humid Tropics: How to Overcome the Cloud Barrier in Greenhouse Gas Remote Sensing, Geophysical Research Letters, 51, https://doi.org/10.1029/2024gl108791, 2024.

https://doi.org/10.5194/egusphere-2026-812
Preprint. Discussion started: 23 February 2026

Fung, I., John, J., Lerner, J., Matthews, E., Prather, M., Steele, L. P., and Fraser, P. J.: Three-dimensional model synthesis of the global methane cycle, Journal of Geophysical Research: Atmospheres, 96, 13 033–13 065, https://doi.org/10.1029/91jd01247, 1991.

Garrigues, S., Chimot, J., Ades, M., Inness, A., Flemming, J., Kipling, Z., Laszlo, I., Benedetti, A., Ribas, R., Jafariserajehlou, S., et al.: Monitoring multiple satellite aerosol optical depth (AOD) products within the Copernicus Atmosphere Monitoring Service (CAMS) data assimilation system, Atmospheric Chemistry and Physics, 22, 14 657–14 692, 2022.

Gorelick, N., Hancher, M., Dixon, M., Ilyushchenko, S., Thau, D., and Moore, R.: Google Earth Engine: Planetary-scale geospatial analysis for everyone, Remote Sensing of Environment, 202, 18–27, https://doi.org/10.1016/j.rse.2017.06.031, 2017.

Gorroño, J., Varon, D. J., Irakulis-Loitxate, I., and Guanter, L.: Understanding the potential of Sentinel-2 for monitoring methane point emissions, Atmospheric Measurement Techniques, 16, 89–107, https://doi.org/10.5194/amt-16-89-2023, 2023.

Hardy, A., Palmer, P. I., and Oakes, G.: Satellite data reveal how Sudd wetland dynamics are linked with globally-significant methane emissions, Environmental Research Letters, 18, 074 044, https://doi.org/10.1088/1748-9326/ace272, 2023.

Janssens-Maenhout, G., Crippa, M., Guizzardi, D., Muntean, M., Schaaf, E., Dentener, F., Bergamaschi, P., Pagliari, V., Olivier, J. G., Peters, J. A., et al.: EDGAR v4. 3.2 Global Atlas of the three major greenhouse gas emissions for the period 1970–2012, Earth System Science Data, 11, 959–1002, 2019.

Jervis, D., McKeever, J., Durak, B. O., Sloan, J. J., Gains, D., Varon, D. J., Ramier, A., Strupler, M., and Tarrant, E.: The GHGSat-D imaging spectrometer, Atmospheric Measurement Techniques, 14, 2127–2140, 2021.

Kurganskiy, A., Feng, L., Humpage, N., Palmer, P. I., Woodwark, A. J. P., Doniki, S., and Weidmann, D.: The Greenhouse gas Emission Monitoring network to Inform Net-zero Initiatives UK (GEMINI-UK): network design, theoretical performance, and initial data, https://doi.org/10.5194/egusphere-2025-94, 2025.

Kvenvolden, K. A. and Rogers, B. W.: Gaia's breath—global methane exhalations, Marine and Petroleum Geology, 22, 579–590, 2005.

Li, D., Cohen, J. B., Qin, K., Xue, Y., and Rao, L.: Absorbing aerosol optical depth from OMI/TROPOMI based on the GBRT algorithm and AERONET data in Asia, IEEE Transactions on Geoscience and Remote Sensing, 61, 1–10, 2022.

Liu, M., van der A, R., van Weele, M., Bryan, L., Eskes, H., Veefkind, P., Liu, Y., Lin, X., de Laat, J., and Ding, J.: Current potential of CH 4 emission estimates using TROPOMI in the Middle East, Atmospheric Measurement Techniques, 17, 5261–5277, 2024.

Lunt, M. F., Palmer, P. I., Feng, L., Taylor, C. M., Boesch, H., and Parker, R. J.: An increase in methane emissions from tropical Africa between 2010 and 2016 inferred from satellite data, Atmospheric Chemistry and Physics, 19, 14 721–14 740, https://doi.org/10.5194/acp-19-14721-2019, 2019.

Lunt, M. F., Palmer, P. I., Lorente, A., Borsdorff, T., Landgraf, J., Parker, R. J., and Boesch, H.: Rain-fed pulses of methane from East Africa during 2018–2019 contributed to atmospheric growth rate, Environmental Research Letters, 16, 024 021, 2021.

Manninen, T., Jääskeläinen, E., Siljamo, N., Riihelä, A., and Karlsson, K.-G.: Cloud-probability-based estimation of black-sky surface albedo from AVHRR data, Atmospheric Measurement Techniques, 15, 879–893, https://doi.org/10.5194/amt-15-879-2022, 2022.

Mao, J., Paulot, F., Jacob, D. J., Cohen, R. C., Crounse, J. D., Wennberg, P. O., Keller, C. A., Hudman, R. C., Barkley, M. P., and Horowitz, L. W.: Ozone and organic nitrates over the eastern United States: Sensitivity to isoprene chemistry, Journal of Geophysical Research: Atmospheres, 118, 11–256, 2013.

Mostafa, M. S. and Du, K.: Satellite-Based Methane Emission Monitoring: A Review Across Industries, Remote Sensing, 17, 3674, 2025.

Palmer, P. I., Wainwright, C. M., Dong, B., Maidment, R. I., Wheeler, K. G., Gedney, N., Hickman, J. E., Madani, N., Folwell, S. S., Abdo, G., et al.: Drivers and impacts of Eastern African rainfall variability, Nature Reviews Earth & Environment, 4, 254–270, 2023.

https://doi.org/10.5194/egusphere-2026-812
Preprint. Discussion started: 23 February 2026

Pendergrass, D. C., Jacob, D. J., Balasus, N., Estrada, L., Varon, D. J., East, J. D., He, M., Mooring, T. A., Penn, E., Nesser, H., and Worden, J. R.: Trends and seasonality of 2019–2023 global methane emissions inferred from a localized ensemble transform Kalman filter (CHEEREIO v1.3.1) applied to TROPOMI satellite observations, Atmospheric Chemistry and Physics, 25, 14 353–14 369, https://doi.org/10.5194/acp-25-14353-2025, 2025.

Qu, Z., Jacob, D. J., Shen, L., Lu, X., Zhang, Y., Scarpelli, T. R., Nesser, H., Sulprizio, M. P., Maasakkers, J. D., Bloom, A. A., et al.: Global distribution of methane emissions: a comparative inverse analysis of observations from the TROPOMI and GOSAT satellite instruments, Atmospheric Chemistry and Physics, 21, 14 159–14 175, 2021.

Saunois, M., Martinez, A., Poulter, B., Zhang, Z., Raymond, P. A., Regnier, P., Canadell, J. G., Jackson, R. B., Patra, P. K., Bousquet, P., Ciais, P., Dlugokencky, E. J., Lan, X., Allen, G. H., Bastviken, D., Beerling, D. J., Belikov, D. A., Blake, D. R., Castaldi, S., Crippa, M., Deemer, B. R., Dennison, F., Etiope, G., Gedney, N., Höglund-Isaksson, L., Holgerson, M. A., Hopcroft, P. O., Hugelius, G., Ito, A., Jain, A. K., Janardanan, R., Johnson, M. S., Kleinen, T., Krummel, P. B., Lauerwald, R., Li, T., Liu, X., McDonald, K. C., Melton, J. R., Mühle, J., Müller, J., Murguia-Flores, F., Niwa, Y., Noce, S., Pan, S., Parker, R. J., Peng, C., Ramonet, M., Riley, W. J., Rocher-Ros, G., Rosentreter, J. A., Sasakawa, M., Segers, A., Smith, S. J., Stanley, E. H., Thanwerdas, J., Tian, H., Tsuruta, A., Tubiello, F. N., Weber, T. S., van der Werf, G. R., Worthy, D. E. J., Xi, Y., Yoshida, Y., Zhang, W., Zheng, B., Zhu, Q., Zhu, Q., and Zhuang, Q.: Global Methane Budget 2000–2020, Earth System Science Data, 17, 1873–1958, https://doi.org/10.5194/essd-17-1873-2025, 2025.

Scarpelli, T. R., Palmer, P. I., Lunt, M., Super, I., and Droste, A.: Verifying national inventory-based combustion emissions of CO 2 across the UK and mainland Europe using satellite observations of atmospheric CO and CO 2, Atmospheric Chemistry and Physics, 24, 10 773–10 791, https://doi.org/10.5194/acp-24-10773-2024, 2024.

Schneising, O., Buchwitz, M., Reuter, M., Bovensmann, H., Burrows, J. P., Borsdorff, T., Deutscher, N. M., Feist, D. G., Griffith, D. W. T., Hase, F., Hermans, C., Iraci, L. T., Kivi, R., Landgraf, J., Morino, I., Notholt, J., Petri, C., Pollard, D. F., Roche, S., Shiomi, K., Strong, K., Sussmann, R., Velazco, V. A., Warneke, T., and Wunch, D.: A scientific algorithm to simultaneously retrieve carbon monoxide and methane from TROPOMI onboard Sentinel-5 Precursor, Atmospheric Measurement Techniques, 12, 6771–6802, https://doi.org/10.5194/amt-12-6771-2019, 2019.

Schneising, O., Buchwitz, M., Hachmeister, J., Vanselow, S., Reuter, M., Buschmann, M., Bovensmann, H., and Burrows, J. P.: Advances in retrieving XCH_4 and XCO from Sentinel-5 Precursor: improvements in the scientific TROPOMI/WFMD algorithm, Atmospheric Measurement Techniques, 16, 669–694, https://doi.org/10.5194/amt-16-669-2023, 2023.

Shaw, J. T., Allen, G., Barker, P., Pitt, J. R., Pasternak, D., Bauguitte, S. J.-B., Lee, J., Bower, K. N., Daly, M. C., Lunt, M. F., et al.: Large methane emission fluxes observed from tropical wetlands in Zambia, Global Biogeochemical Cycles, 36, e2021GB007 261, 2022.

Skeie, R. B., Hodnebrog, , and Myhre, G.: Trends in atmospheric methane concentrations since 1990 were driven and modified by anthropogenic emissions, Communications Earth & Environment, 4, https://doi.org/10.1038/s43247-023-00969-1, 2023.

Suto, H., Kataoka, F., Kikuchi, N., Knuteson, R. O., Butz, A., Haun, M., Buijs, H., Shiomi, K., Imai, H., and Kuze, A.: Thermal and near-infrared sensor for carbon observation Fourier transform spectrometer-2 (TANSO-FTS-2) on the Greenhouse gases Observing SATellite-2 (GOSAT-2) during its first year in orbit, Atmospheric Measurement Techniques, 14, 2013–2039, https://doi.org/10.5194/amt-14-2013-2021, 2021.

Turner, A., Jacob, D. J., Wecht, K. J., Maasakkers, J. D., Lundgren, E., Andrews, A. E., Biraud, S. C., Boesch, H., Bowman, K. W., Deutscher, N. M., et al.: Estimating global and North American methane emissions with high spatial resolution using GOSAT satellite data, Atmospheric Chemistry and Physics, 15, 7049–7069, 2015.

https://doi.org/10.5194/egusphere-2026-812
Preprint. Discussion started: 23 February 2026

Turner, A. J., Frankenberg, C., and Kort, E. A.: Interpreting contemporary trends in atmospheric methane, Proceedings of the National Academy of Sciences, 116, 2805–2813, https://doi.org/10.1073/pnas.1814297116, 2019.

van der Werf, G. R., Randerson, J. T., Giglio, L., van Leeuwen, T. T., Chen, Y., Rogers, B. M., Mu, M., van Marle, M. J. E., Morton, D. C., Collatz, G. J., Yokelson, R. J., and Kasibhatla, P. S.: Global fire emissions estimates during 1997–2016, Earth System Science Data, 9, 697–720, https://doi.org/10.5194/essd-9-697-2017, 2017.

Varon, D. J., Jervis, D., McKeever, J., Spence, I., Gains, D., and Jacob, D. J.: High-frequency monitoring of anomalous methane point sources with multispectral Sentinel-2 satellite observations, Atmospheric Measurement Techniques, 14, 2771–2785, https://doi.org/10.5194/amt-14-2771-2021, 2021.

Virtanen, T. H., Sundström, A.-M., Suhonen, E., Lipponen, A., Arola, A., O'Dell, C., Nelson, R. R., and Lindqvist, H.: A global perspective on CO 2 satellite observations in high AOD conditions, Atmospheric Measurement Techniques Discussions, 2024, 1–40, 2024.

Woodwark, A. J. P. et al.: The Near Infrared Multispectral Camera for Atmospheric Methane (NIMCAM): high spatial resolution methane imaging from space with continuous global coverage, in press, 2026.

Yu, Q., Jervis, D., and Huang, Y.: Accounting for Aerosols Effect in GHGSat Methane Retrieval, EGUsphere, 2024, 1–26, 2024.

Zhang, Y., Jacob, D. J., Lu, X., Maasakkers, J. D., Scarpelli, T. R., Sheng, J.-X., Shen, L., Qu, Z., Sulprizio, M. P., Chang, J., et al.: Attribution of the accelerating increase in atmospheric methane during 2010–2018 by inverse analysis of GOSAT observations, Atmospheric Chemistry and Physics, 21, 3643–3666, 2021.

Zhang, Z., Sherwin, E. D., Varon, D. J., and Brandt, A. R.: Detecting and quantifying methane emissions from oil and gas production: algorithm development with ground-truth calibration based on Sentinel-2 satellite imagery, Atmospheric Measurement Techniques, 15, 7155–7169, https://doi.org/10.5194/amt-15-7155-2022, 2022.

Zhang, Z., Poulter, B., Feldman, A. F., Ying, Q., Ciais, P., Peng, S., and Li, X.: Recent intensification of wetland methane feedback, Nature Climate Change, 13, 430–433, 2023.

https://doi.org/10.5194/egusphere-2026-812
Preprint. Discussion started: 23 February 2026

Appendix A: Probabilistic sub-grid inference of MODIS AOD

To relate MODIS AOD at 1 km resolution to the NIMCAM horizontal resolution of 60 m, we adopt a probabilistic downscaling approach to estimate the number of 60 m pixels with AOD below a given threshold within each 1 km grid cell. For each 1 km cell, we compute a local standard deviation (σ) from the variability of AOD in neighbouring grid cells, which serves as an estimate of sub-grid variability. The reported AOD value is treated as the mean (μ) of a Gaussian distribution. The probability of a 60 m NIMCAM pixel within each 1 km grid cell having AOD below a certain threshold T (e.g., 0.2 or 0.1) is determined by applying the cumulative distribution function (CDF) of the Gaussian distribution:

$$P(AOD < T) = \Phi\left(\frac{T-\mu}{\sigma}\right), \tag{A1}$$

where Φ is the CDF of the standard normal distribution. If σ=0, all sub-grid pixels are assumed to have identical AOD, and the probability is set to 0 or 1 depending on whether μ is below the threshold. Once the probability is calculated, the number of 60 m NIMCAM pixels expected to have AOD below the threshold is found by multiplying the probability by the total number of 60 m NIMCAM pixels in each 1 km cell.

We test our Gaussian assumption by using 15 samples of 60 m resolution AOD data over northern Ghana. Overall, we find our approach effectively predicts the fraction of AOD-free 60 m pixels from 1 km AOD. Fig. A1 summarises the correlation coefficients and biases for all 15 samples. Correlations remain consistently high, with median values of 0.95 and 0.97 for the 0.1 and 0.2 thresholds, respectively. Biases are small, with a median of -0.02 for both thresholds. The bias is predominantly negative, indicating a slight overestimation of the number of AOD-free pixels.

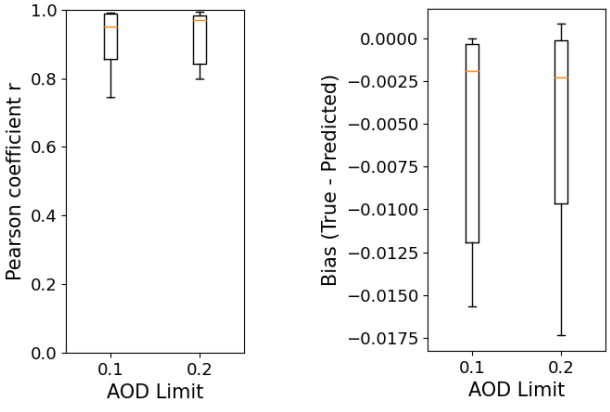

Figure A1. Boxplots showing the range in Pearson correlation, r and mean bias for the 15 processed images.

Fig. A2 shows the analysis on two representative cases of low and high AOD images. The fraction of AOD values below the two thresholds (0.2 and 0.1) within each 1 km grid was computed directly from the the high-resolution 60 m AOD data. Additionally, the 60 m images were downsampled to 1 km resolution, and the fraction of AOD below these thresholds was

https://doi.org/10.5194/egusphere-2026-812
Preprint. Discussion started: 23 February 2026

estimated using the Gaussian approach described above. The observed and predicted fractions exhibit very visually similar distributions, with high correlations and minimal bias.

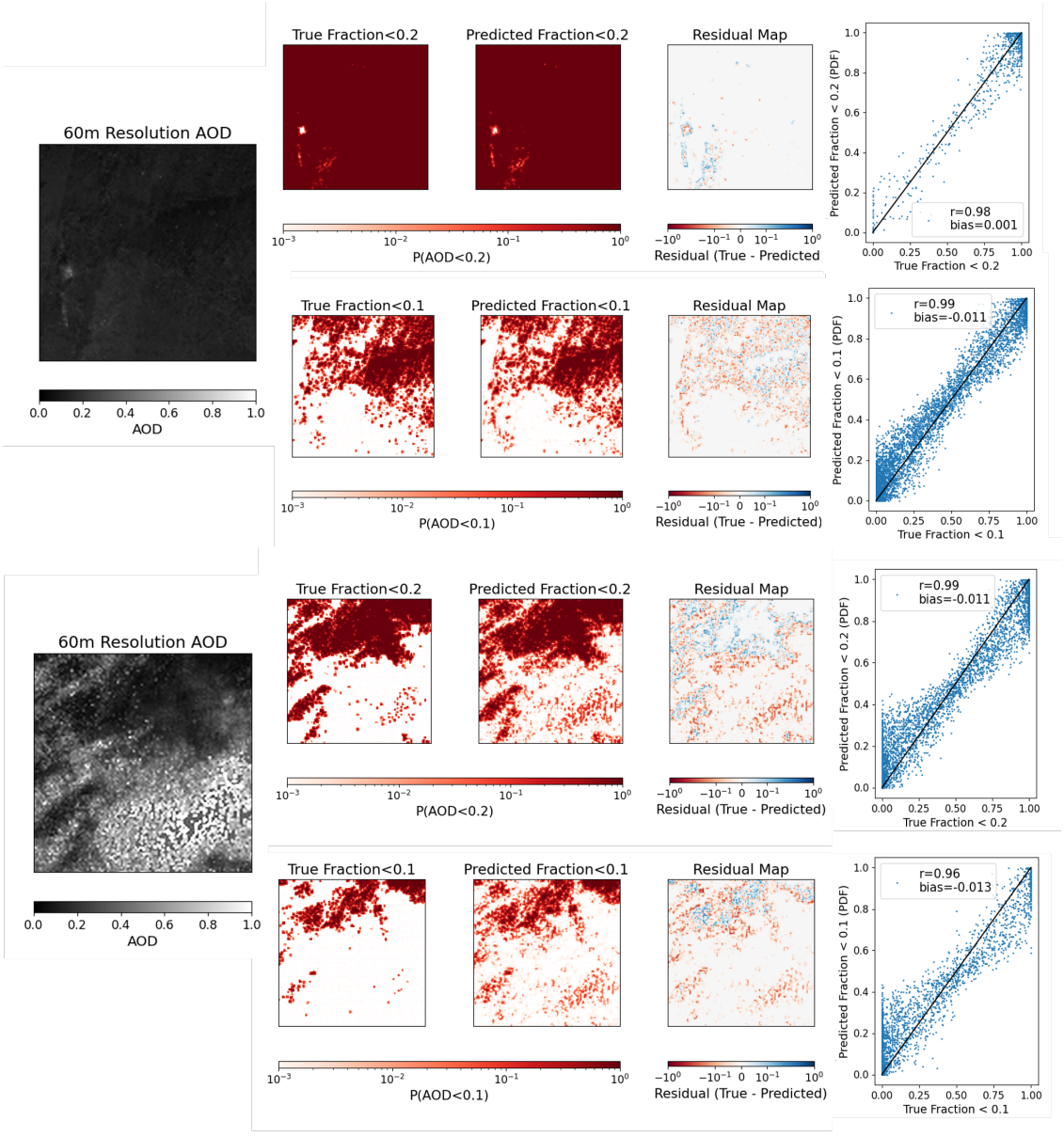

Figure A2. Two examples of high resolution AOD at 60 m. The images are gridded onto a 1km grid and the actual fraction of data <0.2 and <0.1 are counted in each grid. The images are then downsampled to 1 km resolution and the fraction of data <0.2 and <0.1 are predicted using a CDF with Gaussian distribution. The residual map, and scatter plot shows the difference between the true and predicted fractions.

https://doi.org/10.5194/egusphere-2026-812
Preprint. Discussion started: 23 February 2026

Appendix B

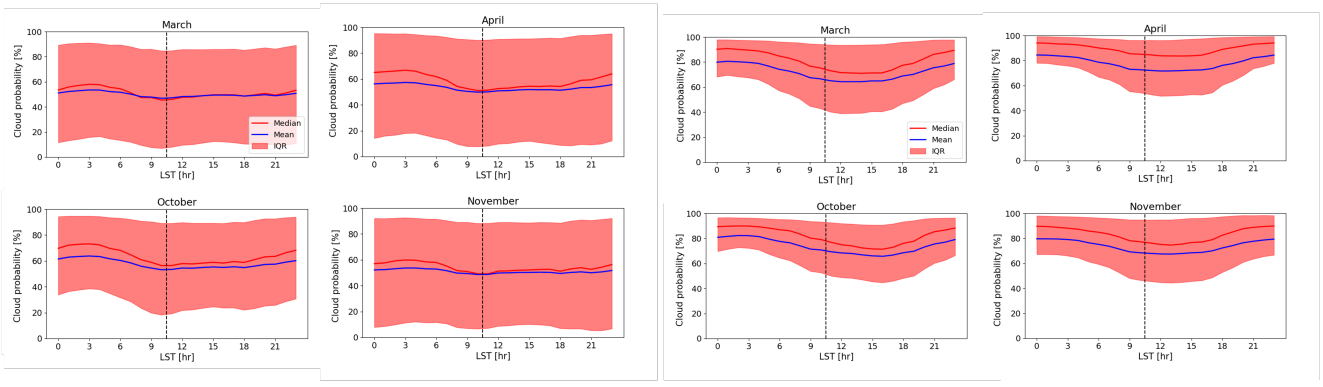

(a) (b)

Figure B1. The diurnal variability in cloud coverage from the GEOS Forward Processing (GEOS-FP) dataset, which provides cloud information at 3 hourly temporal resolution on a 0.25° × 0.3125° spatial resolution. Median (red line), mean (blue line) and IQR (red shaded) cloud fraction plotted against local solar time (LST). Black dashed line marks 10:30, the mean LST of Sentinel-2 overpass (a) Shows the cloud coverage averaged across the full African region, (b) shows the cloud coverage over the Congo Basin (Lat: [-7, 4.5], Lon: [11.5, 30]), which is one of the cloudiest regions in tropical Africa.

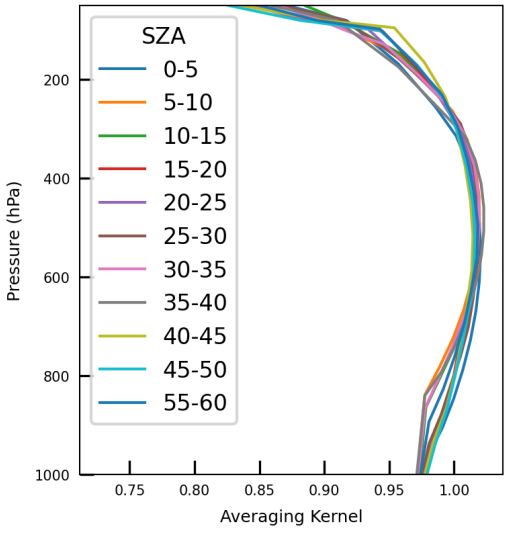

Figure B2. Averaging Kernel profiles used for both NIMCAM and TROPOMI synthetic methane observations. 11 profiles shown binned by solar zenith angle (SZA). Taken from proxy GOSAT XCH_4 retrievals over land.

https://doi.org/10.5194/egusphere-2026-812
Preprint. Discussion started: 23 February 2026

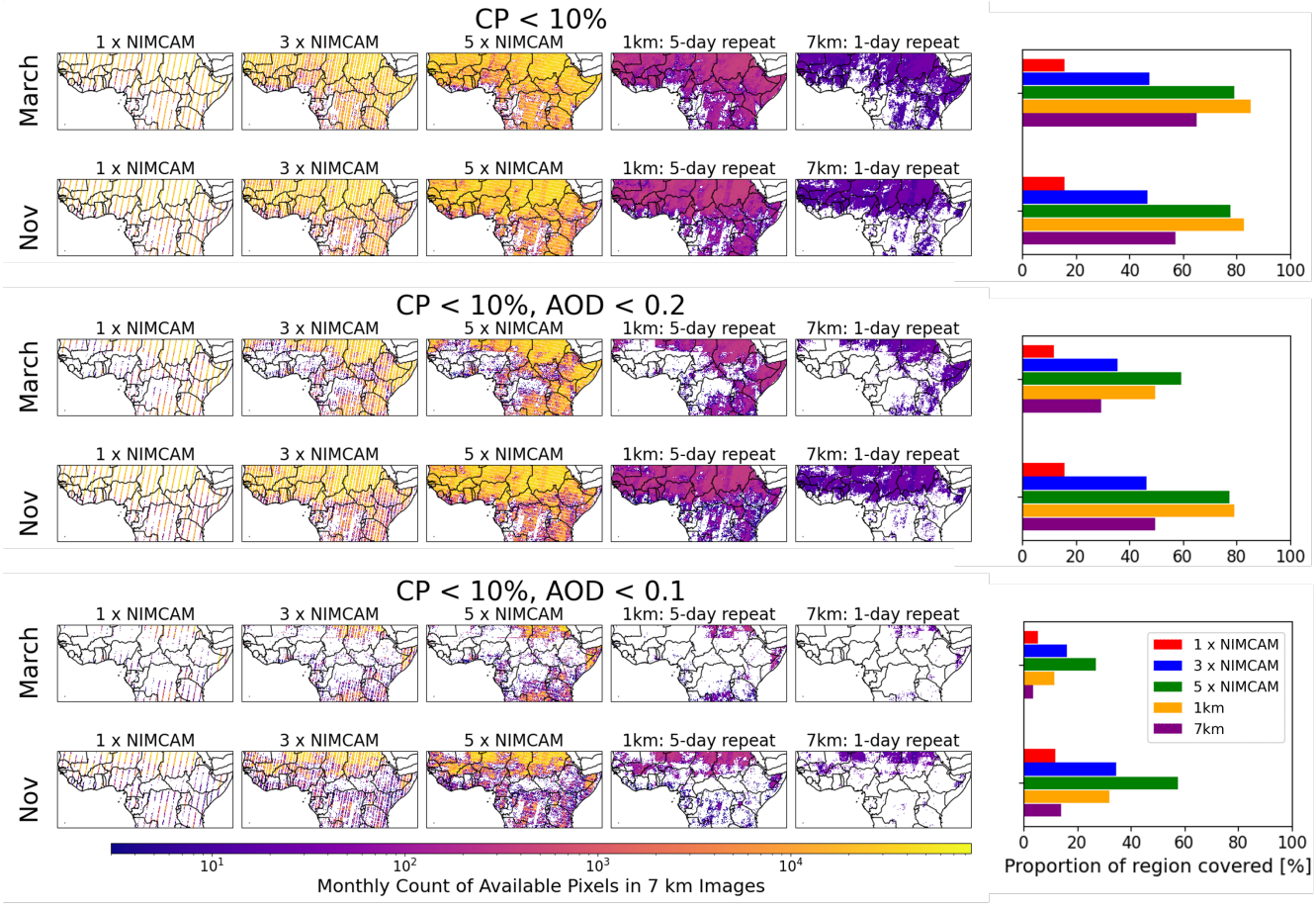

Figure B3. Total pixels recorded in March and November for the NIMCAM IOD and the three and five constellation mission concepts, 1km retrieval (5-day repeat, GOSAT-2), and 7km retrieval (daily repeat, TROPOMI). Compared for cloud masking (CP<10%) and AOD masking (thresholds 0.2 and 0.1). Bar charts show the image availability proportion.